Cu−Fe−Se Ternary Nanosheet-Based Drug Delivery Carrier for Multimodal Imaging and Combined Chemo/Photothermal Therapy of Cancer

Xinxin Jiang, Yaobao Han, Hao Zhang, Hanghang Liu, Qian Huang, Tingting Wang, Qiao Sun, and Zhen Li*

Center for Molecular Imaging and Nuclear Medicine, State Key Laboratory of Radiation Medicine and Protection, School for Radiological and Interdisciplinary Sciences (RAD-X), Soochow University, Collaborative Innovation Center of Radiation Medicine of Jiangsu Higher Education Institutions, Suzhou 215123, China

Ⓢ Supporting Information

ABSTRACT: Ternary transition-metal chalcogenide nanosheets have shown great potential in diverse applications owing to their intrinsically amazing properties with a broad tunable window. Direct preparation of water-soluble and biocompatible ternary chalcogenide nanosheets for theranostic application remains a challenge. In this article, we prepared Cu−Fe−Se nanosheets (CFS NSs) in an aqueous solution under ambient conditions by a sequential coprecipitation method. They were functionalized with anticancer drug doxorubin (CFS@DOX) through electrostatic interactions and labeled with radioactive isotope ^{99m}Tc through surface coordination effect. The resulting nanosheets have a size of 70 nm and a thickness of 5 nm, and can be well dispersed in water, phosphate-buffered saline, 10% fetal bovine serum, and 0.9% NaCl with an excellent colloidal stability. They also exhibit a high photothermal conversion efficiency of 78.9% for in vitro and in vivo photoacoustic imaging and photothermal therapy. The isotope-labeled nanosheets (^{99m}Tc-CFS NSs) were used for single photon emission computed tomography/computed tomography imaging to quantify their blood circulation time (∼4.7 h) and biodistributions in major organs, which follow an order of liver > bladder > lung > spleen > heart > kidney. The DOX-functionalized nanosheets (CFS@DOX) were used for chemotherapy of cancer and exhibited excellent anticancer efficacy. Our research shows the great promise of ternary metal chalcogenide nanosheets for combined imaging and therapy of cancer.

KEYWORDS: two-dimensional ternary nanosheets, transition-metal chalcogenides, photothermal therapy, chemotherapy, radiolabeling, multimodal imaging
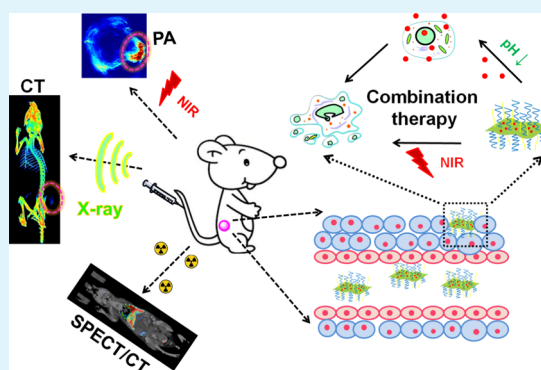
■ INTRODUCTION

Two-dimensional (2D) nanomaterials exhibit excellent chemical, mechanical, thermal, and optical properties, which make them very attractive for diverse applications in energy storage,[1,2] energy conversion,[3−5] electronics,[6,7] catalysis,[8] and sensors.[9,10] In addition, they also harbor diverse strengths for personalized theranostics of cancer, including high uploading of drugs and genes, high photothermal conversion efficiency, and great capability of producing reactive oxygen species.[11] For example, their large surface makes them promising for drug delivery as a large amount of drugs can be loaded on a small amount of nanosheets (NS).[12] Their ultrathin thickness also makes them very sensitive to external stimuli such as light and pH, which was explored for multiresponsive drug release, photothermal therapy (PTT), and photodynamic therapy.[13]

The increasing interest in theranostics of novel 2D nanomaterials with extraordinary physicochemical properties has led to a burst in the development of various 2D materials,[14] in which 2D binary transition-metal chalcogenides (TMCs)

have received significant attention because of their tunable band gaps and versatile properties.[15−17] Various types of binary TMC nanosheets have been fabricated for imaging and therapy of cancer.[18] For example, PEGylated (PEG = poly(ethylene glycol)) WS$_2$ nanosheets were demonstrated to be suitable for computed tomography (CT) and photoacoustic (PA) imaging-guided PTT.[19] Chemically exfoliated MoS$_2$ nanosheets were used as a carrier of doxorubicin (DOX) and applied for combined chemo/photothermal therapy of cancer.[20] TaS$_2$ nanosheets were also proven to be a novel theranostic agent for simultaneous near-infrared (NIR) hyperthermia, chemotherapy, and CT imaging.[21] All these examples clearly demonstrate that 2D TMC nanostructures could be a promising theranostic agent for multimodal imaging and combined therapy.

Scheme 1. (a) Synthesis of Cu−Fe−Se Ternary Nanosheets for Uploading Doxorubicin (CFS@DOX NSs); (b) CFS NSs as a Theranostic Probe for Multimodal Imaging and Combined Chemo/Photothermal Therapy
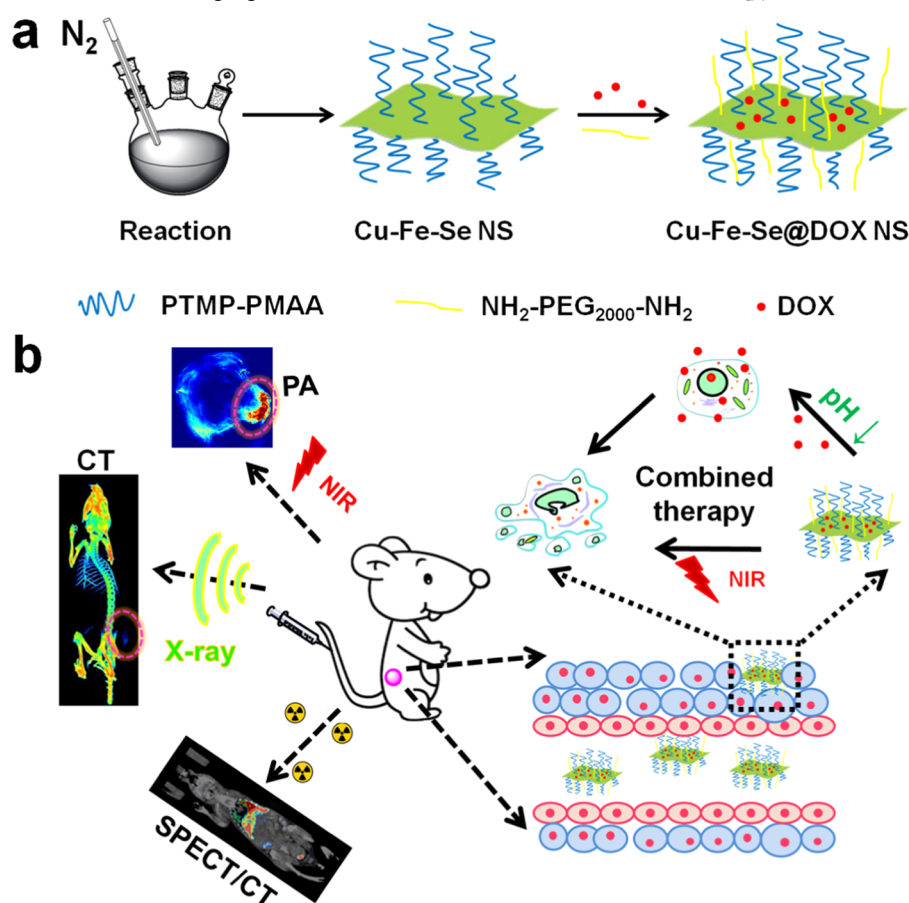

As their elemental components and ratios could significantly influence their intrinsic properties and performance, ternary TMC nanostructures offer a broader spectrum for tuning their functions and applications in comparison with binary ones.[22−26] For example, engineering copper sulfide and selenide with different ratios of Fe^{3+} ions could induce intermediate bands in the fundamental gap and very interesting magnetism.[27−31] The resultant ternary nanostructures, including $CuFeS_2$ nanocrystals,[27] $CuFeS_2$ nanosheets,[28] $CuFeSe_2$ nanocrystals,[29] and Cu_5FeS_4 nanoparticles,[30] have been used not only as an excellent nanotheranostic agent for PA imaging and PTT by taking advantage of their enhanced photothermal conversion property, but also as a contrast agent of magnetic resonance imaging by using their induced magnetism.

In contrast to the abovementioned ternary spherical nanoparticles, there have been only a few reports on 2D ternary nanostructures for biomedical applications because of difficulties in directly synthesizing small water-soluble 2D nanostructures. Most ternary 2D nanostructures usually have been prepared by wet exfoliation of layered bulks, chemical vapor deposition method, or by thermal decomposition of metalorganics in hydrophobic organic solvents, and subsequently modified for bioapplications.[9,18] For instance, $CuFeS_2$ nanoplates were prepared via a thermal decomposition route and then modified with the assistance of cetyltrimethylammonium bromide for synergistic chemo/photothermal therapy.[32] Hence, it is essential to develop an aqueous approach to directly prepare water-soluble and biocompatible nanosheets for combined therapy.

In this article, we show that water-soluble and biocompatible Cu−Fe−Se nanosheets (CFS NSs) can be prepared in aqueous solution under ambient conditions by a sequential coprecipitation method and then functionalized with DOX by electrostatic adsorption (Scheme 1a). The resulting CFS NSs can efficiently convert near-infrared (NIR) light into heat for PA imaging and PTT. They can also act as a contrast agent for CT imaging and for single photon emission computed tomography (SPECT) imaging after they are labeled with radioactive [99m]Tc. In addition, the drug-loaded CFS NSs exhibit drastically enhanced antitumor efficacy by synergistic chemo/photothermal therapy (Scheme 1b).

■ RESULTS AND DISCUSSION

Two-dimensional CFS nanostructures were prepared under ambient conditions and were characterized by transmission electron microscopy (TEM). The irregular flaky nanosheets are around 70 nm (Figure 1a). Their continuous selected area electron diffraction (SAED) pattern in the inset clearly shows the strong diffraction from three planes, which were indexed to be (112), (220), and (200) planes of tetragonal $CuFeSe_2$. Their crystal structure further proved to be tetragonal eskebornite ($CuFeSe_2$, JCPDS no. 81-1959) by X-ray powder diffraction (XRD, Figure 1b). Their thickness was characterized by atomic force microscopy (AFM) to be about 5 nm (Figure 1c,d). The composition and element distribution of these NSs were analyzed by high-angle annular dark field-scanning transmission electron microscopy with energy-
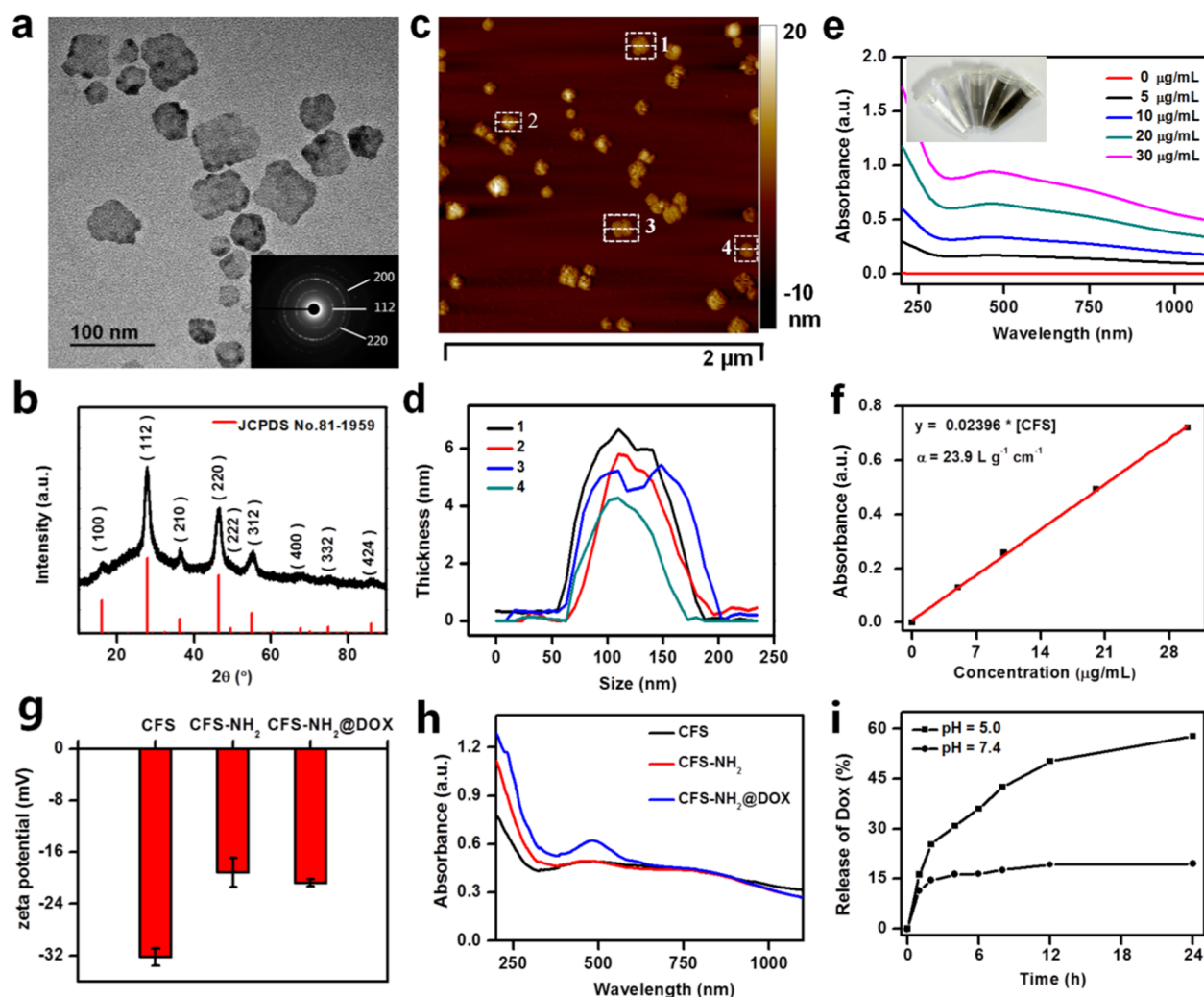
Figure 1. Characterization of as-prepared CFS NSs: (a) TEM image (inset: SAED pattern); (b) XRD pattern with the standard diffractions of cubic berzelianite (JCPDS card no. 81-1959); (c) AFM image; (d) height profiles of the typical nanosheets numbered in (c); (e) UV−vis−NIR absorbance and photograph (inset) of nanosheet solutions with different concentrations; (f) concentration-dependent absorbance of CFS NSs at 808 nm; (g) ζ-potentials; (h) UV−vis−NIR absorbance of CFS, CFS−NH$_2$, and CFS@DOX; and (i) release of DOX from CFS@DOX NSs in buffer solutions at different pH values.

dispersive X-ray spectroscopy, which shows the presence of three elements with uniform distribution throughout the whole nanosheet (Figure S1a in the Supporting Information). The ratio of Cu/Fe/Se in nanosheets is 1.00:0.5:1.06, measured by inductively coupled plasma-optical emission spectrometry (ICP-OES). The redox states of Cu, Fe, and Se elements were characterized to be +1, +3, and −2 (Figure S1b), respectively, according to their binding energies determined by X-ray photoelectron spectroscopy.[33−36] Figure 1e shows photographs and the UV−vis−NIR absorption of CFS NS solutions, in which a unique absorption peak around 500 nm is observed. In addition, their NIR absorbance is much stronger than that of zero-dimensional nanoparticles, which demonstrates the significant influence of morphology on their intrinsic properties. Similar to other nanomaterials, their absorption follows the Lambert−Beer law and linearly increases with their concentration (Figure 1f).[37] Their extinction coefficient at 808 nm (23.9 L g^{-1} cm^{-1}) is 4-fold that of CuFeSe$_2$ nanoparticles (5.8 L g^{-1} cm^{-1}).[29]

Since CFS NSs were stabilized with thiol-functionalized poly(methacrylic acid), their surfaces are strongly negatively charged (Figure 1g) so that they can be simply modified with NH$_2$−PEG$_{2000}$−NH$_2$ and then loaded with DOX via electrostatic interactions. The modified nanosheets (referred to as CFS@DOX NSs) were separated by centrifugation and washed by water several times to remove the free NH$_2$−PEG$_{2000}$−NH$_2$ and DOX. The ζ-potential of the nanosheets changed from −32 to −20 mV after surface modification. In addition, the characteristic absorbance of DOX at 500 nm was clearly observed in the UV−vis−NIR absorption of the CFS@DOX NSs (Figure 1h).[38] The TEM image in Figure S2a shows no obvious difference in the size or morphology of the nanosheets before and after functionalization with DOX. Their Fourier transform infrared spectra further prove the successful modification of nanosheets with both NH$_2$−PEG$_{2000}$−NH$_2$ and DOX (Figure S2b,c). In addition, the release of DOX from CFS@DOX NSs in acidic solution (pH = 5.0) is faster than in physiological solution (pH = 7.4), which is favorable for tumor-targeted drug delivery because of the weakly acidic microenvironment in tumors (Figure 1i). The profile of drug release was fitted with the Wagner log-probability (Figure S3), which is one of the closet models for analysis of multi-
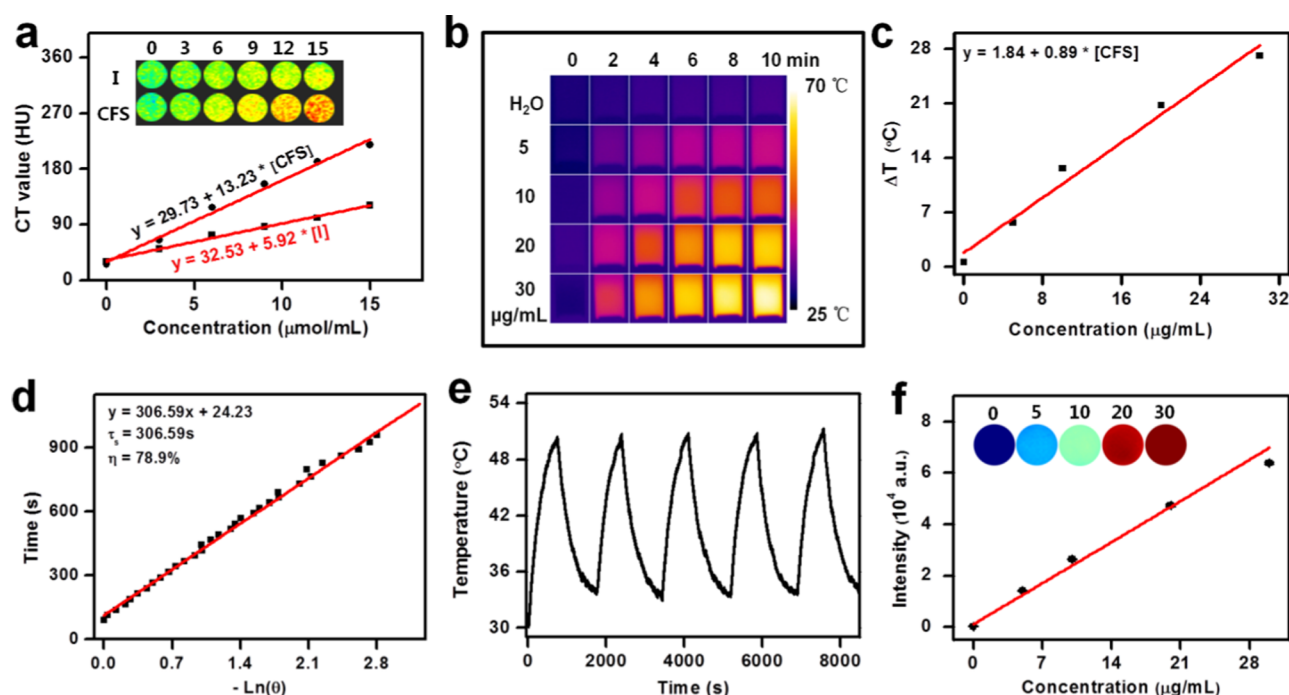
Figure 2. In vitro CT imaging, photothermal conversion, and PA imaging of CFS NSs: (a) CT images (inset) and X-ray attenuation of intensity in Hounsfield units (HU) of CFS NSs as a function of their concentration in contrast to iopromide, (b) photothermal images and (c) the corresponding heating curves of pure water and aqueous solutions of CFS NSs with different concentrations under continuous irradiation by an 808 nm laser with a power density of 0.75 W/cm^2 for 10 min, (d) plot of cooling time (t) versus the negative natural logarithm of the temperature driving force (θ) obtained from the cooling stage as shown in Figure S4b for evaluating the photothermal conversion efficiency (η), (e) temperature variation curve of 1 mL of aqueous solution of CFS NSs (10 μg/mL) recorded during five heating/cooling cycles using an 808 nm laser as the heating source (with a natural cooling process applied following each heating process), and (f) PA images (inset) and the corresponding PA intensity of a series of CFS NS solutions with different concentrations.

mechanistic drug release from nanoparticles.[39−41] The results show that the kinetic constant of the release of DOX in acidic solution was 5.3 times higher than that of in neutral solution.

Previous reports have demonstrated that ternary nanocrystals feature stronger attenuation of X-rays than binary ones as the overall attenuation of X-rays can be considered as the sum of the attenuation of X-rays by individual elements.[42,43] Figure 2a presents the concentration-dependent Hounsfield unit (HU) values of the CFS NSs and the clinical CT agent (the inset is their CT images), in which the signals of their CT images are positively linearly increased with their concentration, and the slope of the CFS NSs (13.23 HU L/mmol) is 2-fold that of the clinically used iopromide (I) (5.92 HU L/mmol). This result suggests the potential of CFS NSs in CT imaging.

As mentioned previously, the introduction of Fe^{3+} ions into copper chalcogenides could induce intermediate bands in the fundamental gap, leading to dramatic enhancement of the photothermal conversion efficiency.[27] Figures 2b,c and S4a display that the temperature of the nanosheet solutions is increased with concentration increasing from 0 to 30 μg/mL after laser irradiation and shows a positive linear relationship. To measure the photothermal conversion efficiency (η),[44,45] we used an 808 nm laser to irradiate 1 mL of CFS NS solution (10 μg/mL) to achieve the maximum temperature and then cooled it naturally to room temperature (Figure S4b). The η was calculated to be 78.9% (Figure 2d) by a method reported previously.[46] To examine its photothermal stability, we heated and cooled a CFS NS solution (10 μg/mL) for five cycles, in each of which the laser was turned on to heat the nanosheet

solution for 10 min and then turned off. The similar temperature profiles of the five cycles illustrate their excellent photothermal stability (Figure 2e). Their excellence in photothermal conversion indicates their potential in PA imaging, which has been proven in vitro (Figure 2f). The PA signal linearly increases with concentration of CFS NSs.

All the above characterization demonstrates that CFS NSs could be used for multimodal imaging-guided chemo/photothermal therapy of cancer if they are safe and biocompatible. The hydrodynamic sizes of CFS NSs and CFS@DOX NSs dispersed in different media (i.e., water, phosphate-buffered saline (PBS), 10% fetal bovine serum, and 0.9% NaCl) for 5 days were recorded to verify their stability in a simulated biological environment (Figure S5a,b). Except for a slight increase in PBS and 0.9% NaCl, they retained good stability in other cases, indicating that CFS NSs could be used for in vivo applications. Their biocompatibility was assessed by the standard 3-(4,5-dimethylthiazol-2-yl)-2,5-diphenyltetrazolium bromide assay, in which CFS NSs exhibited some toxicity at higher concentrations (i.e., >12.5 μg/mL). At the same concentration, CFS@DOX NSs were much more toxic than CFS NSs because of additional DOX carried by those nanosheets (Figure 3a). Furthermore, the cytotoxicities of polymer ligand and DOX indicate that pentaerythritol tetrakis 3-mercaptopropionate−poly(methacrylic acid) was safe for surface modification and that DOX was an effective antitumor drug (Figure S6a,b).

The dependence of cellular uptake on the nanosheets and culture time was quantified by ICP-OES measurements. The results indicate that when the cells were cultured with different
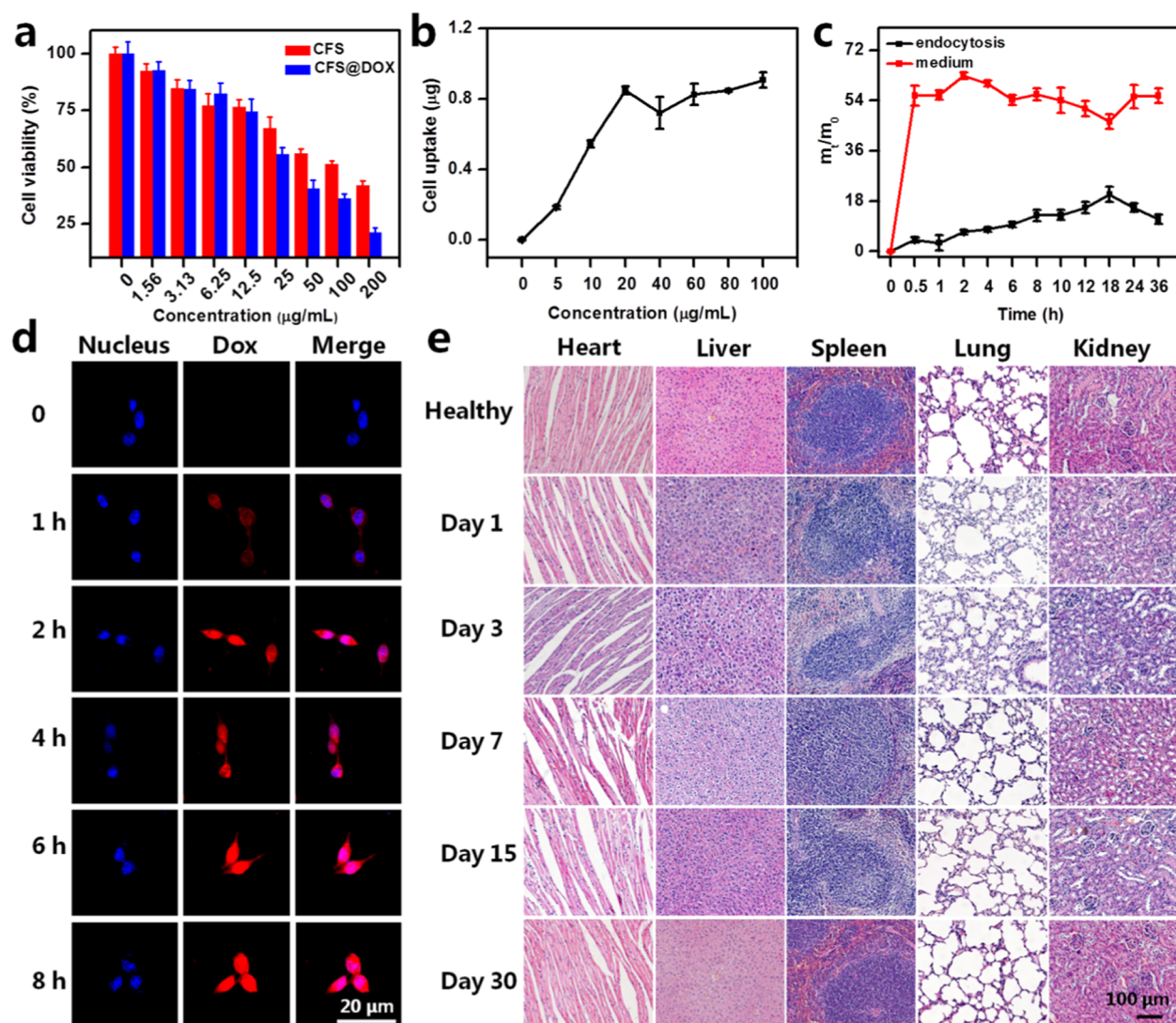
Figure 3. (a) Relative viabilities of 4T1 cells after incubation with CFS NSs and CFS@DOX NSs at different concentrations for 24 h, (b) endocytosis of different concentrations of CFS NSs by 4T1 cells, (c) ratios of CFS NSs endocytosed by the cells and in the culture media, and (d) confocal fluorescence images of 4T1 cells after incubation with CFS@DOX NSs for 0, 1, 2, 4, 6, and 8 h. Red and blue represent the fluorescence of DOX and that of cell nuclei stained with 4,6-diamidino-2-phenylindole, respectively. (e) Hematoxylin and eosin (H&E) staining of major organs sectioned from healthy mice sacrificed on days 1, 3, 7, 15, and 30 after injection of CFS@DOX NSs.

concentrations of CFS NSs for 12 h, the ideal concentration of nanosheets for cells to achieve the highest uptake was 20 μg/mL (Figure 3b), and when 20 μg/mL CFS NS solution was incubated with the cells for different times, the optimal culture time for cells to maximally phagocytose the nanosheets was 18 h (Figure 3c). In addition, the PA images of cells incubated with different concentrations of CFS NSs or for different times show the same results (Figure S7a,b). After optimization of the nanosheet concentration and culture time, the endocytosis of CFS@DOX NSs by 4T1 cells and the release of DOX in the cells were investigated. Figure 3d shows the gradual intracellular release of DOX, as evidenced by the gradual variation and diffusion of the characteristic red fluorescence from DOX. The results also indicate that DOX was released into the cytoplasm within the initial 1 h and then diffused into the nucleus.

To assess their in vivo biosafety, 200 μL of CFS@DOX NSs (2 mg/mL) was intravenously administrated into healthy female mice through their tail veins. Their main organs were

excised for sectioning and hematoxylin and eosin (H&E) staining at 1, 3, 7, 15, and 30 days after the injection of nanosheets and compared with those of untreated healthy mice (Figure 3e). The nuclei of the hepatic cells became larger on day 1 and day 3 and then recovered to normal on day 7, indicating that the reticuloendothelial cells in the liver phagocytosed a large amount of CFS@DOX NSs, which caused cell necrosis within the first 3 days due to an immune stress reaction.[47] There was no abnormality in other organs (i.e., heart, spleen, lung, and kidney) in comparison with healthy organs.

The above results demonstrate low toxicity of our CFS@DOX NSs. Their pharmacokinetics were then assessed by quantification of γ-rays from SPECT/CT images because of their very high sensitivity (10^{-10}–10^{-12} mol/mL). CFS NSs were labeled with radioactive ^{99m}Tc (subsequently referred to as ^{99m}Tc-CFS NSs), which did not cause any change in their hydrodynamic size (Figure S8a). The labeled nanosheets were intravenously injected into a tumor-bearing mouse (7.5 mg/kg,
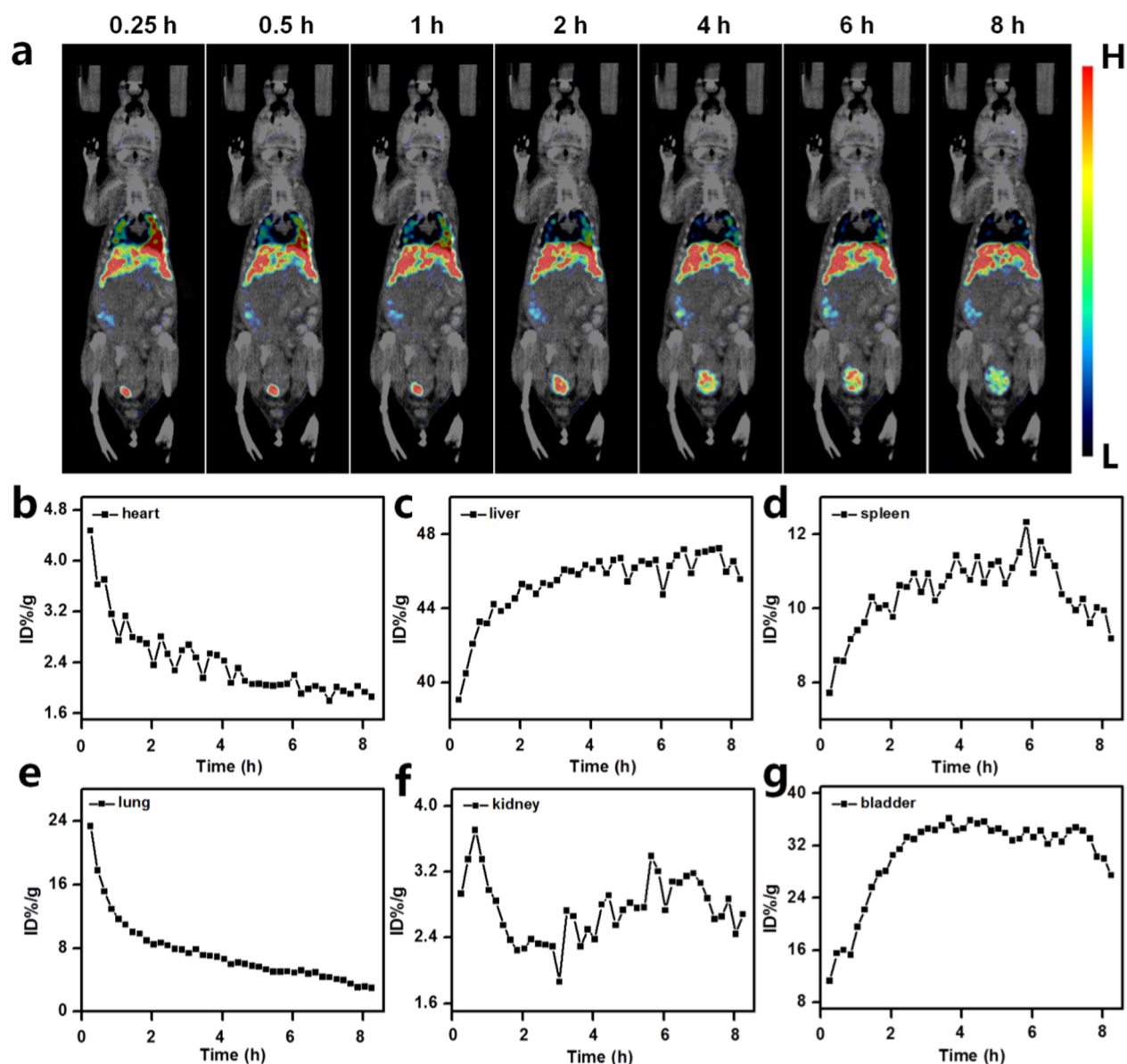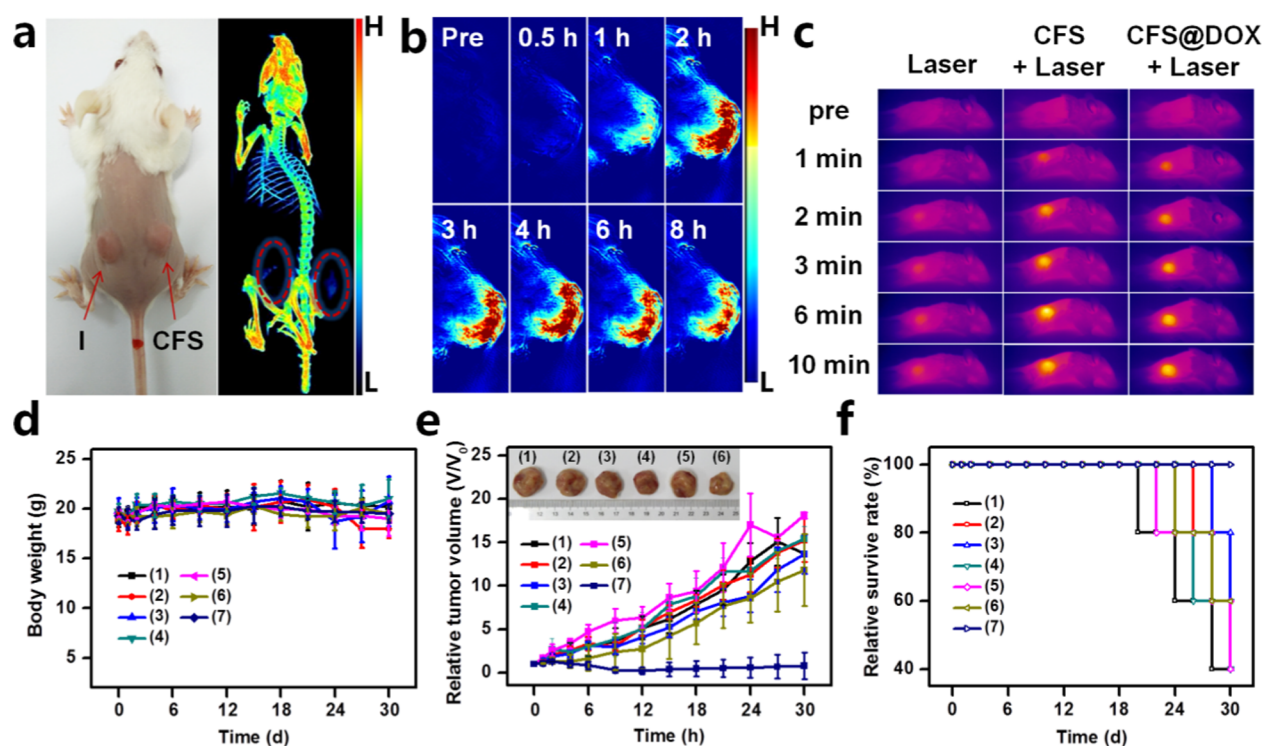
Figure 4. (a) SPECT/CT images of a mouse bearing a tumor at different times after intravenous injection of CFS NSs, and (b−g) time-dependent pharmacokinetics of ^{99m}Tc-CFS NSs in different organs: (b) heart, (c) liver, (d) spleen, (e) lung, (f) kidney, and (g) bladder.

400 μCi ^{99m}Tc), and their blood circulation time was quantified to be 4.7 h by fitting the intensity of the γ-rays on the heart (Figure S8b). The absence of γ-emission at the thyroid gland of the mouse (Figure 4a) indicates the negligible dissociation of ^{99m}Tc from nanosheets.

The distributions of labeled nanosheets in the other organs were quantified similarly. The signal intensity of γ-rays in the liver increased quickly in the first 2 h after injection of ^{99m}Tc-CFS NS solution, and the γ-emissions were the strongest among the major organs. Obviously, the liver serves as an important organ for the clearance of foreign substances through phagocytosis and provides the critical functions of metabolism and biliary excretion of nanosheets.[48] The distribution of nanosheets in other organs followed the order of bladder > lung > spleen > heart > kidney (Figure 4b−g). Parts of the ^{99m}Tc-CFS NSs were quickly cleared in the first 4 h and excreted through the bladder. In addition, ^{99m}Tc-CFS NSs accumulated in the heart and lungs were quickly metabolized within 2 h. The nanosheets in the spleen increased

first and then decreased, indicating their gradual accumulation and metabolization. These results demonstrate that our CFS@DOX NSs were mainly captured by the reticuloendothelial system (RES) due to their large particle size and negatively charged surface. The RES is a network of cells located throughout the body that helps filter out dead and toxic particles and also works to identify foreign substances in both the blood and tissues.

The above results demonstrate the feasibility of quantifying the biodistribution of nanosheets by the highly sensitive SPECT/CT imaging. Compared with a conventional method such as ICP-mass spectrometry, this approach not only saved many mice, but also provided real-time dynamics with higher reliability. Therefore, SPECT/CT imaging is an ideal option for quantifying the pharmacokinetics of nanomaterials in animals. In addition to SPECT/CT imaging, CT imaging and PA imaging of tumors were carried out with our nanosheets to show their potential in multimodal imaging. A mouse bearing two tumors on both sides of the thigh was used for CT

Figure 5. (a) Photograph (left) and 3D in vivo CT image (right) of a mouse bearing two tumors, which were intratumorally injected with CFS NSs and iopromide, respectively; (b) in vivo PA images of tumor acquired at different times after the mouse was intravenously injected with CFS NSs; (c) infrared thermal images collected at different times post injection of 4T1 tumor-bearing mice intravenously injected with CFS NS and CFS@ DOX NS solutions, respectively, and then irradiated with an 808 nm NIR laser at a power density of 1 W/cm² for 10 min, in comparison with tumor-bearing mice injected with PBS solution followed by NIR irradiation; (d) average body weights of mice from each group after various treatments: (1) control, without treatment; (2) CFS, injection of CFS NSs only; (3) DOX, injection of free DOX; (4) CFS@DOX, injection of CFS@DOX NSs; (5) laser, irradiation with laser only; (6) CFS + Laser, injection of CFS NSs and irradiation with laser; (7) CFS@DOX + laser, injection of CFS@DOX NSs and irradiation with laser; (e) relative volumes of tumors (photographs in inset) after the above treatments, normalized to their initial volumes; (f) survival rates of different groups of mice after the various treatments.

imaging. The right tumor was injected with CFS NSs (25 mg/kg), and the left tumor was injected with the same dose of iopromide (I) for comparison. The three-dimensional (3D) CT image in Figure 5a shows that the signal in the right tumor was 2 times higher than that in the left one, as analyzed with PMOD image quantitative analysis software (Figure S9a). The PA imaging was performed on a tumor-bearing nude mouse over 8 h with the multispectral PA imaging system (MSOT inSight) after the mouse was intravenously injected with nanosheets. The intensity of the PA images of tumor was the strongest at 2 h post injection and then gradually weakened (Figures 5b and S9b), which suggests that the best treatment time was 2 h post injection.

To demonstrate the performance of CFS@DOX NSs for combined chemo/photothermal therapy, the tumor-bearing mice were randomly classified into seven groups: (1) control group without treatment; (2) CFS NSs group; (3) free DOX group; (4) CFS@DOX NSs group; (5) laser group; (6) PTT group (CFS NSs + Laser); and (7) combined therapy group (CFS@DOX NSs + Laser). The time-dependent temperatures of tumors from the latter three groups of mice irradiated by an 808 nm laser are shown in Figures 5c and S9c. For the mice treated with CFS NSs or CFS@DOX NSs, the temperature of their tumors was increased from ∼35.1 to ∼54.1 °C after they were irradiated for 10 min. However, the temperature of tumors of mice from the laser group was slightly increased to 40.9 °C. In the following month after treatment, the mice were photographed, weighed, had their tumor volume measured,

and their survival status recorded every two or three days. There was a slight difference in their weights in the first two weeks, but after that, the weights of the mice gradually decreased with the growth of the tumor (Figure 5d). The pictures of mice in Figure S10 also show the changes in the tumor. Except for the combined therapy group, the tumors in the other groups kept growing, and the mice eventually died. For the mice treated with PTT only, their tumor shrunk in the first week and then continued to grow (Figure 5e). The results demonstrate the significance of combined therapy.

The rapid growth of the tumors consumed a large amount of nutrients in mice and led to increasingly worse immunity in the mice, which caused infection and loss of function in some organs, eventually resulting in the death of the mice. During the period of observation, the mice from groups 1−5 died subsequently, and some mice from group 6 also died (Figure 5f). For humanitarian reasons, all the mice were sacrificed after 30 days, and their major organs were harvested for observation. The observation of tumor cells in the liver and lung and their irregular distribution in mice from groups 1−6 suggest metastasis of the tumors (Figure S11, black circle). It is noteworthy that the mice from group 7 recovered gradually after the combined chemo/photothermal therapy by using CFS@DOX NSs. Their tumors sloughed off, accompanied by the growth of new skin and hair. Their organs were observed to have similarity to that of healthy ones. The results demonstrate the great potential of CFS@DOX NSs in combined chemo/photothermal therapy.

CONCLUSIONS

In summary, we successfully prepared Cu−Fe−Se ternary nanosheets in an aqueous solution under ambient conditions by the sequential coprecipitation method in the presence of thiol-functionalized poly(methacrylic acid). The resultant nanosheets are 70 nm in diameter and 5 nm in thickness. They can be well dissolved in different media with excellent colloidal stability due to the negatively charged surface and the steric effect of the polymer ligand. They also show excellent photothermal conversion property, which was used for PA imaging to determine the optimal time window for treatment. Their negative charged surface and multifunctional groups make them attractive for uploading anticancer drugs and for labeling with radioactive isotopes for SPECT/CT imaging. The unique 2D structure and properties make them ideally suitable for multimodal theranostic agents for multimodal imaging and combined chemo/photothermal therapy, of which the former imaging was used to quantify the pharmacokinetics of nanosheets and drugs and the latter therapy was used to successfully kill cancer cells. Although only a small amount of nanosheets could reach the tumor site by the EPR effect, they are enough for the imaging and therapy. This work demonstrates the promise of ternary metal chalcogenide nanosheets in theranostics of cancer. Reducing their accumulation in major organs and improving their accumulation in tumor through active targeting to achieve better efficacy will be our next goal.

ASSOCIATED CONTENT

ⓢ Supporting Information

The Supporting Information is available free of charge on the ACS Publications website at DOI: 10.1021/acsami.8b15064.

> Details of experiments, characterization of nanosheets, photographs of mice from different treatments, and histological images of their tissue sections (PDF)

AUTHOR INFORMATION

Corresponding Author
*E-mail: zhenli@suda.edu.cn.

ORCID ⓘ
Zhen Li: 0000-0003-0333-7699

Author Contributions
X.J., Y.H., H.Z., H.L., Q.H., and T.W. did the experiments, collected and analyzed results, and prepared the manuscript draft. Q.S. and Z.L. designed the experiments and mentored students to perform experiments. All authors discussed the results and commented on the manuscript.

Notes
The authors declare no competing financial interest.

ACKNOWLEDGMENTS

REFERENCES

(1) Anasori, B.; Lukatskaya, M. R.; Gogotsi, Y. 2D Metal Carbides and Nitrides (Mxenes) for Energy Storage. *Nat. Rev. Mater.* 2017, 2, No. 16098.

(2) Han, C.; Li, Z.; Li, W. J.; Chou, S. L.; Dou, S. X. Controlled Synthesis of Copper Telleride Nanostructures for Long-cycling Anode in Lithium Ion Batteries. *J. Mater. Chem. A* 2014, 2, 11683−11690.

(3) Han, C.; Bai, Y.; Sun, Q.; Zhang, S. H.; Li, Z.; Wang, L. Z.; Dou, S. X. Ambient Aqueous Growth of Cu₂Te Nanostructures with Excellent Electrocatalytic Activity towards Sulfide Redox Shuttles. *Adv. Sci.* 2016, 3, No. 1500350.

(4) Chen, X. Q.; Li, Z.; Bai, Y.; Sun, Q.; Wang, L. Z.; Dou, S. X. Room-Temperature Synthesis of Cu₂₋ₓE (E = S, Se) Nanotubes with Hierarchical Architecture as High-Performance Counter Electrodes of Quantum-Dots-Sensitized Solar Cells. *Chem. - Eur. J.* 2015, 21, 1055−1063.

(5) Chen, X. Q.; Li, Z.; Dou, S. X. Ambient Facile Synthesis of Gram-Scale Copper Selenide Nanostructures From Commercial Copper and Selenium Powder. *ACS Appl. Mater. Interfaces* 2015, 7, 13295−13302.

(6) Ding, X.; Feng, X.; Saeki, A.; Seki, S.; Nagai, A.; Jiang, D. Conducting Metallophthalocyanine 2d Covalent Organic Frameworks: The Role of Central Metals in Controlling Pi-Electronic Functions. *Chem. Commun.* 2012, 48, 8952−8954.

(7) Dong, G. P.; Zhang, Y. H.; Pan, Q. W.; Qiu, J. R. A Fantastic Graphitic Carbon Nitride (G -C₃N₄) Material: Electronic Structure, Photocatalytic and Photoelectronic Properties. *J. Photochem. Photobiol., C* 2014, 20, 33−50.

(8) Yan, Z. L.; Fu, L. J.; Zuo, X. C.; Yang, H. M. Green Assembly of Stable and Uniform Silver Nanoparticles on 2D Silica Nanosheets for Catalytic Reduction of 4-Nitrophenol. *Appl. Catal., B* 2018, 226, 23−30.

(9) Wang, L.; Xiong, Q. R.; Xiao, F.; Duan, H. W. 2d Nanomaterials Based Electrochemical Biosensors for Cancer Diagnosis. *Biosens. Bioelectron.* 2017, 89, 136−151.

(10) Zhang, Y.; Zheng, B.; Zhu, C. F.; Zhang, X.; Tan, C. L.; Li, H.; Chen, B.; Yang, J.; Chen, J. Z.; Huang, Y.; Wang, L. H.; Zhang, H. Single-Layer Transition Metal Dichalcogenide Nanosheet-Based Nanosensors for Rapid, Sensitive, and Multiplexed Detection of DNA. *Adv. Mater.* 2015, 27, 935−939.

(11) Chen, Y.; Wu, Y. K.; Sun, B. B.; Liu, S. J.; Liu, H. Y. Two-Dimensional Nanomaterials for Cancer Nanotheranostics. *Small* 2017, 13, No. 1603446.

(12) Chou, S. S.; Kaehr, B.; Kim, J.; Foley, B. M.; De, M.; Hopkins, P. E.; Huang, J.; Brinker, C. J.; Dravid, V. P. Chemically Exfoliated MoS₂ as near-Infrared Photothermal Agents. *Angew. Chem., Int. Ed.* 2013, 52, 4160−4164.

(13) Zhu, X.; Ji, X. Y.; Kong, N.; Chen, Y. H.; Mahmoudi, M.; Xu, X. D.; Ding, L.; Tao, W.; Cai, T.; Li, Y. J.; Gan, T.; Barrett, A.; Bharwani, Z.; Chen, H. B.; Farokhzad, O. C. Intracellular Mechanistic Understanding of 2D MoS₂ Nanosheets for Anti-Exocytosis-Enhanced Synergistic Cancer Therapy. *ACS Nano* 2018, 12, 2922−2938.

(14) Chen, W.; Ouyang, J.; Liu, H.; Chen, M.; Zeng, K.; Sheng, J.; Liu, Z.; Han, Y.; Wang, L.; Li, J.; Deng, L.; Liu, Y. N.; Guo, S. Black Phosphorus Nanosheet-Based Drug Delivery System for Synergistic Photodynamic/Photothermal/Chemotherapy of Cancer. *Adv. Mater.* 2017, 29, No. 1603864.

(15) Chhowalla, M.; Shin, H. S.; Eda, G.; Li, L. J.; Loh, K. P.; Zhang, H. The Chemistry of Two-Dimensional Layered Transition Metal Dichalcogenide Nanosheets. *Nat. Chem.* 2013, 5, 263−275.

(16) Tan, C.; Zhang, H. Two-Dimensional Transition Metal Dichalcogenide Nanosheet-Based Composites. *Chem. Soc. Rev.* 2015, 44, 2713−2731.

(17) Chhowalla, M.; Liu, Z. F.; Zhang, H. Two-Dimensional Transition Metal Dichalcogenide (TMD) Nanosheets. *Chem. Soc. Rev.* 2015, 44, 2584−2586.

(18) Kalantar-zadeh, K.; Ou, J. Z.; Daeneke, T.; Strano, M. S.; Pumera, M.; Gras, S. L. Two-Dimensional Transition Metal

Dichalcogenides in Biosystems. *Adv. Funct. Mater.* **2015**, *25*, 5086−5099.

(19) Cheng, L.; Liu, J. J.; Gu, X.; Gong, H.; Shi, X. Z.; Liu, T.; Wang, C.; Wang, X. Y.; Liu, G.; Xing, H. Y.; Bu, W. B.; Sun, B. Q.; Liu, Z. Pegylated WoS₂ Nanosheets as a Multifunctional Theranostic Agent for in Vivo Dual-Modal Ct/Photoacoustic Imaging Guided Photothermal Therapy. *Adv. Mater.* **2014**, *26*, 1886−1893.

(20) Liu, T.; Wang, C.; Gu, X.; Gong, H.; Cheng, L.; Shi, X. Z.; Feng, L. Z.; Sun, B. Q.; Liu, Z. Drug Delivery with Pegylated MoS₂ Nano-Sheets for Combined Photothermal and Chemotherapy of Cancer. *Adv. Mater.* **2014**, *26*, 3433−3440.

(21) Liu, Y.; Ji, X.; Liu, J.; Tong, W. W. L.; Askhatova, D.; Shi, J. Tantalum Sulfide Nanosheets as a Theranostic Nanoplatform for Computed Tomography Imaging-Guided Combinatorial Chemo-Photothermal Therapy. *Adv. Funct. Mater.* **2017**, *27*, No. 1703261.

(22) Kim, J. H.; Oh, S.; Sohn, W. H.; Rhyee, J.-S.; Park, S.-D.; Kang, H.; Ahn, D. Thermoelectric, Thermodynamic, and Structural Properties in Cu₁.₉₄A₀.₀₂Se (A = Al, Ga, and In) Polycrystalline Compounds. *Acta. Mater.* **2015**, *100*, 32−38.

(23) Wang, C.; Hu, Z. Y.; Xu, S. H.; Wang, Y. B.; Zhao, Z. X.; Wang, Z. Y.; Cui, Y. P. Tuning the Emission of Aqueous Cu:ZnSe Quantum Dots to Yellow Light Window. *Nanotechnology* **2015**, *26*, No. 305601.

(24) Liu, X.; Swihart, M. T. Heavily-Doped Colloidal Semiconductor and Metal Oxide Nanocrystals: An Emerging New Class of Plasmonic Nanomaterials. *Chem. Soc. Rev.* **2014**, *43*, 3908−3920.

(25) Han, C.; Sun, Q.; Cheng, Z. X.; Wang, J. L.; Li, Z.; Lu, G. Q.; Dou, S. X. Ambient Scalable Synthesis of Surfactant-free Thermoelectric CuAgSe Nanoparticles with Reversible Metallic-n-p Conductivity Transition. *J. Am. Chem. Soc.* **2014**, *136*, 17626−17633.

(26) Chen, X. Q.; Bai, Y.; Sun, Q.; Li, Z.; Wang, L. Z.; Dou, S. X. Ambient Synthesis of One-Dimensional/Two-Dimensional CuAgSe Ternary Nanotubes as High-Performance Counter Electrodes of Quantum-Dot-Sensitized Solar Cells. *ChemPlusChem* **2015**, *81*, 414−420.

(27) Ghosh, S.; Avellini, T.; Petrelli, A.; Kriegel, I.; Gaspari, R.; Almeida, G.; Bertoni, G.; Cavalli, A.; Scotognella, F.; Pellegrino, T.; Manna, L. Colloidal CuFeS₂ nanocrystals: Intermediate Fe d-Band Leads to High Photothermal Conversion Efficiency. *Chem. Mater.* **2016**, *28*, 4848−4858.

(28) Li, Y.; Wang, Y.; Pattengale, B.; Yin, J.; An, L.; Cheng, F. Y.; Li, Y.; Huang, J.; Xi, P. X. High-Index Faceted CuFeS₂ Nanosheets with Enhanced Behavior for Boosting Hydrogen Evolution Reaction. *Nanoscale* **2017**, *9*, 9230−9237.

(29) Jiang, X.; Zhang, S. H.; Ren, F.; Chen, L.; Zeng, J. F.; Zhu, M.; Cheng, Z. X.; Gao, M. Y.; Li, Z. Ultrasmall Magnetic CuFeSe₂ Ternary Nanocrystals for Multimodal Imaging Guided Photothermal Therapy of Cancer. *ACS Nano* **2017**, *11*, 5633−5645.

(30) Zhao, Q.; Yi, X.; Li, M. F.; Zhong, X. Y.; Shi, Q. L.; Yang, K. High near-Infrared Absorbing Cu₅FeS₄ Nanoparticles for Dual-Modal Imaging and Photothermal Therapy. *Nanoscale* **2016**, *8*, 13368−13376.

(31) Zhang, S.; Huang, Q.; Zhang, L. J.; Zhang, H.; Han, Y. B.; Sun, Q.; Cheng, Z. X.; Qin, H. Z.; Dou, S. X.; Li, Z. Vacancy Engineering of Cu₂₋ₓSe Nanoparticles with Tunable LSPR and Magnetism for Dual-modal Imaging Guided Photothermal Therapy of Cancer. *Nanoscale* **2018**, *10*, 3130−3143.

(32) Ding, B.; Yu, C.; Li, C. X.; Deng, X. R.; Ding, J. X.; Cheng, Z. X.; Xing, B. G.; Ma, P.; Lin, J. Cis-Platinum Pro-Drug-Attached CuFeS₂ Nanoplates for in Vivo Photothermal/Photoacoustic Imaging and Chemotherapy/Photothermal Therapy of Cancer. *Nanoscale* **2017**, *9*, 16937−16949.

(33) Reddy, K. V.; Chetty, S. C. Mössbauer Studies on CuFeSe₂. *Mater. Res. Bull.* **1976**, *11*, 55−60.

(34) Wang, W.; Jiang, J.; Ding, T.; Wang, C. D.; Zuo, J.; Yang, Q. Alternative Synthesis of CuFeSe₂ Nanocrystals with Magnetic and Photoelectric Properties. *ACS Appl. Mater. Interfaces* **2015**, *7*, 2235−2241.

(35) Hamdadou, N.; Morsli, M.; Khelil, A.; Bernède, J. C. Fabrication of N- and P-Type Doped CuFeSe₂ Thin Films Achieved by Selenization of Metal Precursors. *J. Phys. D: Appl. Phys.* **2006**, *39*, 1042−1049.

(36) Zhang, H.; Wang, T. T.; Qiu, W. B.; Han, Y. B.; Sun, Q.; Zeng, J. F.; Yan, F.; Zheng, H. R.; Li, Z.; Gao, M. Y. Monitoring the Opening and Recovery of the Blood-Brain-Barrier with Non-invasive Molecular Imaging by Biodegradable Ultrasmall Cu₂₋ₓSe Nanoparticles. *Nano Lett* **2018**, *18*, 4985−4992.

(37) Huang, S. S.; He, Q. Q.; Chen, W. L.; Zai, J. T.; Qiao, Q. Q.; Qian, X. F. 3d Hierarchical FeSe₂ Microspheres: Controlled Synthesis and Applications in Dye-Sensitized Solar Cells. *Nano Energy* **2015**, *15*, 205−215.

(38) Yi, X.; Chen, L.; Chen, J.; Maiti, D.; Chai, Z. F.; Liu, Z.; Yang, K. Biomimetic Copper Sulfide for Chemo-Radiotherapy: Enhanced Uptake and Reduced Efflux of Nanoparticles for Tumor Cells under Ionizing Radiation. *Adv. Funct. Mater.* **2018**, *28*, No. 1705161.

(39) Matthaiou, E. I.; Barar, J.; Sandaltzopoulos, R.; Li, C.; Coukos, G.; Omidi, Y. Shikonin-loaded antibody-armed nanoparticles for targeted therapy of ovarian cancer. *Int. J. Nanomed.* **2014**, *1*, No. 1855.

(40) Barzegar-Jalali, M.; Adibkia, K.; Valizadeh, H.; Shadbad, M. R.; Nokhodchi, A.; Omidi, Y.; et al. Kinetic analysis of drug release from nanoparticles. *J. Pharm. Pharm. Sci.* **2008**, *11*, 167−177.

(41) Del Fresno, C.; Saz-Leal, P.; Enamorado, M.; Wculek, S. K.; Martínez-Cano, S.; Blanco-Menéndez, N.; Planas, A.; et al. DNGR-1 in dendritic cells limits tissue damage by dampening neutrophil recruitment. *Science* **2018**, *362*, 351−356.

(42) Mao, F.; Wen, L.; Sun, C. X.; Zhang, S. H.; Wang, G. L.; Zeng, J. F.; Wang, Y.; Ma, J. M.; Gao, M. Y.; Li, Z. Ultrasmall Biocompatible Bi₂Se₃ Nanodots for Multimodal Imaging-Guided Synergistic Radiophotothermal Therapy against Cancer. *ACS Nano* **2016**, *10*, 11145−11155.

(43) Wen, L.; Chen, L.; Zheng, S. M.; Zeng, J. F.; Duan, G. X.; Wang, Y.; Wang, G. L.; Chai, Z. F.; Li, Z.; Gao, M. Y. Ultrasmall Biocompatible WO₃₋ₓ Nanodots for Multi-Modality Imaging and Combined Therapy of Cancers. *Adv. Mater.* **2016**, *28*, 5072−5079.

(44) Zhang, S.; Sun, C. X.; Zeng, J. F.; Sun, Q.; Wang, G. L.; Wang, Y.; Wu, Y.; Dou, S. X.; Gao, M. Y.; Li, Z. Ambient Aqueous Synthesis of Ultrasmall Pegylated Cu₂₋ₓSe Nanoparticles as a Multifunctional Theranostic Agent for Multimodal Imaging Guided Photothermal Therapy of Cancer. *Adv. Mater.* **2016**, *28*, 8927−8936.

(45) Sun, C.; Wen, L.; Zeng, J. F.; Wang, Y.; Sun, Q.; Deng, L. J.; Zhao, C. J.; Li, Z. One-Pot Solventless Preparation of Pegylated Black Phosphorus Nanoparticles for Photoacoustic Imaging and Photothermal Therapy of Cancer. *Biomaterials* **2016**, *91*, 81−89.

(46) Zhu, H.; Wang, Y.; Chen, C.; Ma, M. R.; Zeng, J. F.; Li, S. Z.; Xia, Y. S.; Gao, M. Y. Monodisperse Dual Plasmonic Au@Cu₂₋ₓE (E = S, Se) Core@Shell Supraparticles: Aqueous Fabrication, Multimodal Imaging, and Tumor Therapy at in Vivo Level. *ACS Nano* **2017**, *11*, 8273−8281.

(47) Kleiner, D. E. The Pathology of Drug-Induced Liver Injury. *Semin. Liver. Dis.* **2009**, *29*, 364−372.

(48) Longmire, M.; Choyke, P. L.; Kobayashi, H. Clearance Properties of Nano-Sized Particles and Molecules as Imaging Agents: Considerations and Caveats. *Nanomedicine* **2008**, *3*, 703−717.